# Plasmonic Transition via Interparticle Coupling of Au@Ag Core–Shell Nanostructures Sheathed in Double Hydrophilic Block Copolymer for High-Performance Polymer Solar Cell

Eunyong Seo,[§,†] Seo-Jin Ko,[§,†] Sa Hoon Min,[†] Jin Young Kim,*[,†] and Byeong-Su Kim*[,†,‡]

[†]Department of Energy Engineering and [‡]Department of Chemistry, Ulsan National Institute of Science and Technology (UNIST), Ulsan 689-798, Korea

S *Supporting Information*

ABSTRACT: We herein report a facile synthetic method for the preparation of gold-core, silver-shell nanoparticles (Au@Ag NPs) with tunable surface plasmon resonance (SPR) using the double hydrophilic block copolymer (DHBC), poly(ethylene oxide)-*block*-poly(acrylic acid) (PEO-*b*-PAA), as a template (Au@Ag@DHBC NPs), and the utilization of their unique optical properties in polymer solar cells (PSCs). It is demonstrated that two different functionalities of DHBC facilitate the formation of the respective Au-core and Ag-shell NPs. Interestingly, the isolated core–shell NPs in solution are found to be transformed into coupled NPs that ultimately exhibit the transition of intrinsic plasmonic properties to a wide range in the visible spectrum. Furthermore, plasmonic Au@Ag@DHBC NPs are effectively integrated into the active layer of PSCs, which remarkably enhance the power conversion efficiency (PCE) up to 9.0% (16% enhancement) because of the strong plasmonic effect of the coupled NPs and the thin polymeric layer surrounding the NPs. This study suggests the widespread potential application of DHBCs as a template for the synthesis of novel core–shell nanostructures. We anticipate that this approach will provide new means for creating a variety of plasmonic nanomaterials in various fields of optoelectronic devices.
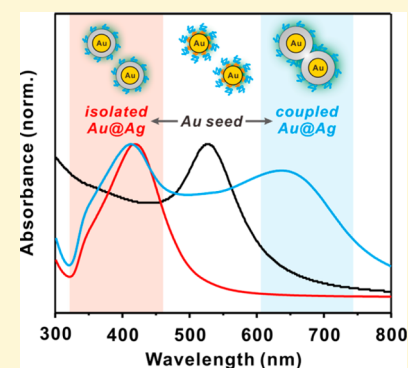
INTRODUCTION

The emergence of plasmonics in nanoscale materials has renewed interests in the fundamental understanding of localized surface plasmons, which arise from collective and coherent oscillations of the conduction electrons in resonance with the incident light frequency on the surface of a metal nanoparticle (NP).[1−3] The creation and examination of numerous metal NPs have demonstrated the importance of each parameter, such as size, shape, and assembly, on tailoring their intrinsic plasmonic characteristics.[4−15] Novel metal nanostructures and their alloys have been the subject of intensive research owing to their interesting plasmonic behavior, including localized surface plasmon resonance (LSPR), surface-enhanced Raman scattering (SERS), and metal-enhanced fluorescence, which are useful for various applications toward biosensors, bioimaging, catalysis, thermal therapy, and optoelectronic devices, such as solar cells and light emitting diodes.[16−22]

In particular, plasmonic metal NPs have received significant attention in polymer solar cells (PSCs) applications because their LSPR effect can lead to enhancement of incident light absorption and improvement of intrinsic scattering power for higher efficiency of solar cells. Among many novel metal NPs, gold and silver possess very effective plasmonic effects to trap incident light, which exhibit relatively strong scattering in the visible range.[23,24] However, attempts at obtaining high efficiency in PSCs by employing the SPR effect are limited because of the narrow resonant wavelength region of metal

nanostructures.[2] In addition, direct integration of metal NPs into the active layer of PSCs often leads to exciton quenching in the system,[25,26] which inevitably requires surface passivation of the metal NPs.[18] In order to overcome these challenges associated with plasmonic metal NPs, it is essential to modulate the spectrum of light absorption, to improve the generation of excitons, and to prevent exciton quenching or recombination to maximize the plasmon effect on device performance.[27−31]

Numerous approaches to design the plasmonic properties of novel metal nanostructures, attributed to their size, shape, and morphology, have been reported using specific surfactants or polymer capping methods. As an alternative to the traditional surfactant-based approach, block copolymer-templated syntheses can offer interesting opportunities not only for forming inorganic NPs with a controllable size and shape but also for stabilizing the resulting NPs by forming steric or ionic barriers around the NPs in solution.[32−34] Furthermore, this block copolymer-based method offers a means to direct the spatial patterning of NPs on the surface as a result of their unique self-assembly behavior.[35−38]

Most block copolymer self-assembly approaches rely on the use of entirely hydrophobic or amphiphilic block copolymers, forming various micellar structures in solution similar to the self-assembly of surfactants. On the other hand, double

hydrophilic block copolymers (DHBCs) consisting of two chemically distinct segments with only hydrophilic features have recently stood out in the preparation of NPs.[39−41] Compared with the hydrophobic block copolymer, all hydrophilic block copolymers show unique features in aqueous solution; for example, they dissolve readily in water to form molecularly dissolved solutions and induce potentially useful micellar aggregates with inorganic materials through polyion complexation in aqueous solution. These materials are important for the design of "nano-reactors" with DHBCs for ionic substances compared to the micelles of conventional amphiphilic block copolymers.[42]

To date, only a few reports using DHBCs for the preparation of metallic NPs have been achieved as a result of the limited tunability of size, shape, or morphology. This DHBC-based synthetic approach to novel nanostructures is thus challenging because the micellization with inorganic materials via various types of polymer blocks and the corresponding mineralization for the formation of NPs are effectively controlled by many parameters such as temperature, ionic strength, pH variation, and complexation in aqueous solution.[42,43] Additionally, two different functional groups in DHBCs can be utilized to produce nanostructures, such as core−shell shapes, consisting of two or more metallic components via the seed-mediated method. In a DHBC system, one block typically exhibits a positive or negative charge in aqueous solution, which can interact with the metal precursor. On the other hand, the other block is typically neutral but can be also employed as an active site assisting the NPs growth if oxygen atoms with abundant lone pair electrons are contained in the segment.

In this context, a DHBC-based synthesis of metal NPs offers a straightforward and versatile method to produce core−shell nanostructures under mild aqueous conditions without the use of organic solvents or thermal treatment. Furthermore, this report can shed new light on the diverse functionalities of DHBC, including (1) guidance for the controlled growth of core−shell structure, (2) coupling agent between NPs, (3) passivation for efficient introduction of surface plasmon effect directly in device, and (4) more importantly, protective layer against the energy transfer on device.

Herein, we report the synthesis of Au@Ag NPs using a soft DHBC template to prepare core−shell NPs and investigate their potential as plasmonic nanomaterials in PSCs. Specifically, the DHBC of poly(ethylene oxide)-*block*-poly(acrylic acid) (PEO-*b*-PAA) provides spherical Au NPs (Au@DHBC NPs) resulting from its micellar structure in aqueous solution.[44] Afterward, the Ag shell can be selectively grown on top of the Au@DHBC NPs because the PEO block interacts with the Ag^+ ions, leading to the Au@Ag@DHBC core−shell nanostructures. The shell thickness is simply controlled by the Ag precursor concentration; thus, the plasmon properties of Au@Ag@DHBC NPs become highly tunable. Most interestingly, interparticle coupling is observed with the addition of high concentration of Ag^+ ions, leading to the transition of intrinsic plasmon bands of isolated individual Au@Ag@DHBC NPs to a wide range in the visible spectrum. Furthermore, coupled NPs are successfully employed as plasmonic nanomaterials to improve the light absorption window of the photoactive layer in PSCs, improving their efficiency by ∼16%. Owing to the two different functional groups in the DHBC, this DHBC-based approach not only provides a unique alternative to the existing methods for preparation of core−shell metal nanostructures but

also allows for the tuning of the SPR effect of novel NPs over a broad range for improved efficiency in optoelectronic devices.

■ EXPERIMENTAL SECTION

Materials. Double hydrophilic block copolymer PEO(5000)-*b*-PAA(6700) was purchased from Polymer Source, Inc. Gold(III) chloride trihydrate ($HAuCl_4 \cdot 3H_2O$), silver nitrate ($AgNO_3$), and L-ascorbic acid (AA) from Sigma-Aldrich and sodium hydroxide (NaOH) from Junsei Chemical were used without further purification.

Synthesis of Au@DHBC NPs. Au NPs with a double hydrophilic block copolymer shell (Au@DHBC NPs) were prepared according to the following protocol.[44] First, PEO(5000)-*b*-PAA(6700) (25.12 mg, 0.20 mmol of carboxylic acid groups) was dissolved under vigorous stirring in 50.0 mL of deionized water, followed by the addition of 0.10 mL of 4.0 M NaOH (0.40 mmol, 2 equiv. of carboxylic acid groups in PAA block). To this solution, 4.47×10^{-3} M $HAuCl_4 \cdot 3H_2O$ (26.2 mg, 0.067 mmol) was added. Subsequently, 2.0 mL of 1.0 M AA (2.0 mmol) was added to the resulting suspension under vigorous stirring. After a few minutes, the solution underwent a color change to transparent red. After the reaction, the solution was dialyzed against deionized water using a dialysis membrane (MWCO 12 000−14 000, SpectraPore) to remove any residuals. The prepared suspension of Au@DHBC NPs exhibited fairly good colloidal stability, which lasted more than 6 months without any precipitation.

Synthesis of Au@Ag@DHBC NPs. Gold−silver−DHBC core−shell nanostructures (Au@Ag@DHBC NPs) were synthesized via a seed-mediated method. As-prepared Au@DHBC NPs were used as seeds for the growth. A solution of as-synthesized Au@DHBC NPs (0.5 mL) was first diluted with a certain amount of water, followed by the addition of different amounts of Ag precursor ranging from 0.2 to 2.0 μmol into the solution with the total volume fixed at 1.5 mL. As-synthesized Au@Ag NPs by DHBC are denoted Au@Ag$_n$@DHBC, where n is the number of moles of Ag precursor used for the synthesis of the NPs. For example, when 0.1 and 1.0 μmol of Ag precursor is employed in the reaction, the NPs are denoted as Au@Ag$_{0.1}$@DHBC and Au@Ag$_{1.0}$@DHBC, respectively.

Characterization. The morphology, size, and size distribution of the prepared NPs were investigated using transmission electron microscopy (TEM), high-angle annular dark field scanning transmission electron microscopy (HAADF-STEM), and energy dispersive X-ray spectroscopy (EDXS) (JEOL, JEM-2100F, accelerating voltage of 200 kV, Gatan CCD camera). UV−vis spectra were recorded using a UV−vis spectrophotometer (Shimadzu UV-1800), and size distribution analyses were performed using dynamic light scattering (DLS, BI-APD, Brookhaven Instruments, New York, U.S.A.).

Fabrication and Characterization of Solar Cells. Devices were fabricated according to the following procedure. First, the ITO/glass substrates were cleaned with detergent, then ultrasonicated in acetone and isopropyl alcohol, and subsequently dried in an oven overnight at 100 °C. Poly(3,4-ethylenedioxythiophene):polystyrenesulfonate (PEDOT:PSS) layers, which were used as the anode, were spin-coated (after passing through a 0.45 μm cellulose acetate syringe filter) at 5000 rpm for 40 s, followed by baking at 145 °C for 10 min in air. A solution of Au@Ag@DHBC NPs was spin-coated on top of the PEDOT:PSS layer and then baked at 60 °C for 5 min. For deposition of the active layer, a blend solution of poly[4,8-bis(5-(2-ethylhexyl)-thiophen-2-yl)benzo[1,2-b:4,5-b′] dithiophene-*co*-3-fluorothieno[3,4-b] thiophene-2-carboxylate] (PTB7-Th) (1 wt %):[6,6]-phenyl-C_{71}-butyric acid methyl ester (PC$_{71}$BM) (1.5 wt %) dissolved in chlorobenzene with 3 vol % diphenylether was spin-coated on top of the PEDOT:PSS layer in a nitrogen-filled glovebox. The device was pumped down in a vacuum ($<10^{-6}$ Torr; 1 Torr = 133 Pa), and a 100 nm thick Al electrode, for convention, was deposited on top of the active layer by thermal evaporation. The deposited Al electrode area defined the active area of the device as 13 mm^2. Measurements were performed with the solar cells inside the glovebox by using a high-quality optical fiber to guide the light from the solar simulator equipped with a Keithley 2635A source measurement unit. The $J−V$ curves for the devices were measured under AM 1.5 G illumination at

Scheme 1. Schematic Illustration of the Synthesis of Au−Ag Core-Shell NPs Using a Double Hydrophilic Block Copolymer Template (Au@Ag@DHBC NPs) and Isolated and Coupled Au@Ag@DHBC NPs via a Seed Growth Method Determined by the Concentration of Ag Precursor
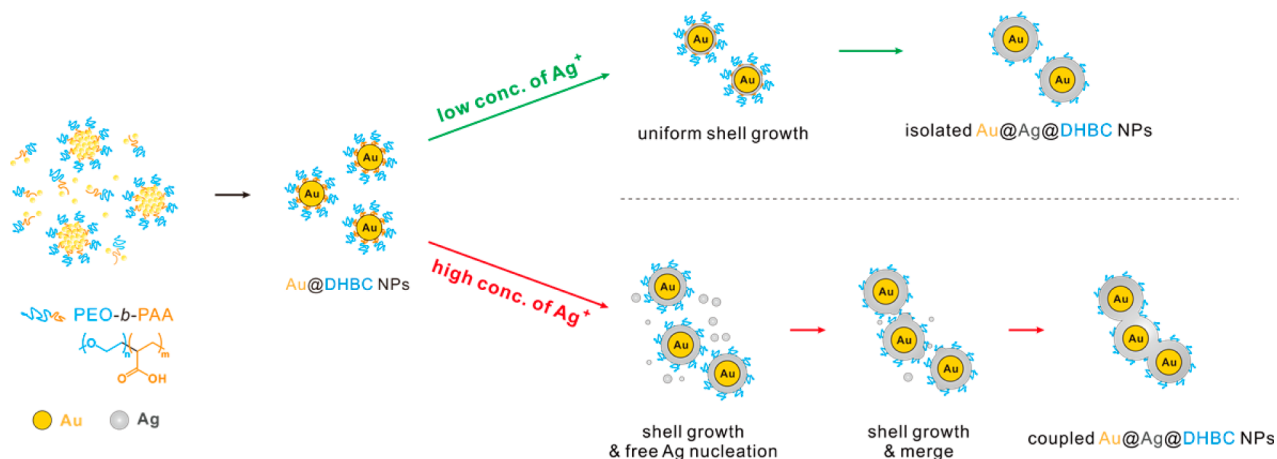
100 mW/cm^2 with masking. External quantum efficiency (EQE) measurements were also conducted in ambient air using an EQE system (Model QEX7) by PV Measurements Inc. (Boulder, Colorado). After collecting the EQE data, the software also integrated the data with the AM 1.5 G spectrum and reported the calculated J_{SC} values.

Simulation of Electric Field Distribution. The E-field enhancement and extinction cross-section for Au@Ag@DHBC NPs were calculated by a finite-difference time-domain (FDTD) method (FDTD Solutions 8.6, Lumerical). The numerical simulations were performed in a three-dimensional box with a cell size of 0.1 nm and perfectly matched layers for all boundaries. For the Au@Ag@DHBC core−shell NP model, the diameter and interparticle spacing of the NPs were adjusted according to the TEM observations. The dielectric functions of Au, Ag, and DHBC in the UV−vis region were described by a multicoefficient fitted model of the experimental data by Palik.[45] The Au@Ag@DHBC NPs were illuminated by a total-field/scattered-field plane wave source to obtain the extinction cross section as a function of wavelength by calculating the absorption and scattering cross sections.

■ RESULTS AND DISCUSSION

The syntheses of Au@DHBC and Au@Ag@DHBC NPs are illustrated in Scheme 1. The initial synthetic procedure for Au NPs as a core material was modified from the method reported in our previous research.[44] In the preparation of Au NPs by DHBC, the PAA block facilitates the micellar formation by interacting with the metal precursor, followed by forming spherical Au nanostructure with an average diameter of 17.0 ± 4.1 nm and a surface plasmon band at 522 nm (Figure 1a and Supporting Information Figure S1). Simultaneously, the PEO block provides steric stabilization for the resulting Au@DHBC NPs, which are stable for a few months without any aggregation.

We then employed the Au@DHBC NPs as a seed to further synthesize core−shell nanostructures via the following process. Briefly, the Au@DHBC NPs solution is mixed with different concentrations of Ag precursor, followed by the addition of a reducing agent into the mixture to grow the Ag shell with various thicknesses on top of the Au@DHBC NPs. As-prepared core−shell NPs are denoted as Au@Ag$_n$@DHBC NPs, where n represents the moles of Ag precursor added to the Au seed solution (typically $n = 0.1−2.0$ μmol). As shown in Figure 1b,c, the Au core and Ag shell portions are clearly distinguishable due to their electron density contrast. Additional high-
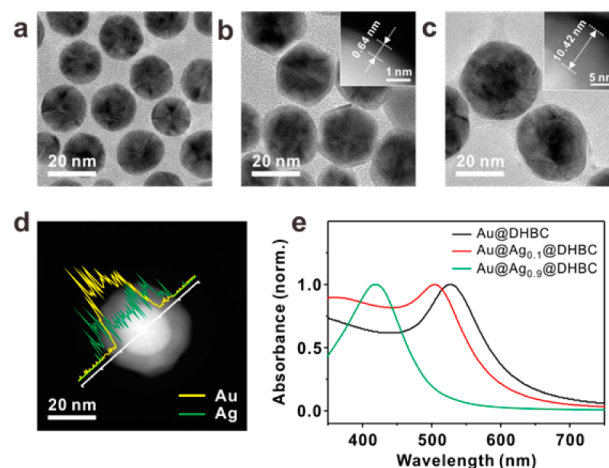

Figure 1. Isolated Au@Ag NPs by DHBC. TEM images of (a) Au@DHBC NPs and (b, c) Au@Ag@DHBC NPs synthesized by 0.1 and 0.9 μmol AgNO$_3$, denoted as Au@Ag$_{0.1}$@DHBC NPs and Au@Ag$_{0.9}$@DHBC NPs, respectively. Inset figures in b and c show the dark field STEM images of Au@Ag@DHBC NPs. (d) Compositional line profiles of representative Au@Ag@DHBC NPs shown in c. (e) UV−vis spectra of Au@DHBC NPs and Au@Ag@DHBC NPs.

resolution dark field HADDF STEM images included in the inset of Figure 1 and Supporting Information Figure S2 clearly indicate a boundary between Au core and Ag shell with varying shell thickness. In addition, both the compositional line profiles (Figure 1d) and the corresponding energy dispersive spectrum (EDS) point analysis (Supporting Information Figure S3) confirm the presence of Au and Ag located in the core and shell, respectively. Upon the formation of the Ag shell on top of Au@DHBC NPs, the original surface plasmon band at 522 nm gradually blue-shifted toward 505 nm (Au@Ag$_{0.1}$@DHBC NPs) and 419 nm (Au@Ag$_{0.9}$@DHBC NPs), which is characteristic of the LSPR of spherical Ag NPs.

It is worth noting that no free Ag NPs were found after the formation of the core−shell of Au@Ag@DHBC NPs. It has been previously reported that PEO plays an important role not only in forming sterically stabilized NPs in solution but also in guiding the reduction of Ag ions into metallic Ag NPs.[46,47] The role of oxygen atoms in reducing the metal salts is similarly demonstrated in the case of polyvinylpyrrolidone (PVP) in

creating NPs with various structures.[48,49] Similarly, in our system, the PEO block in DHBC provides an active site to bind with the Ag ions due to the lone pair electrons on oxygen, leading to the ion-dipole interaction between the Ag ions and the polymer. This interaction facilitates the formation of Ag shell on the surface of Au seed because PAA block binding with Au core cannot participate in the reaction of Ag ions, and simultaneously PEO block exposed out of core interacts with Ag ions. We therefore highlight the significant role of DHBC in creating core–shell type nanostructures in a controllable manner to form a shell on top of Au@DHBC seeds.

Upon the formation of the Ag shell on top of Au@DHBC NPs, the solution of Au@Ag@DHBC NPs exhibits a progressive color transition from red to yellow and orange (Figure 2a), as similarly observed in color changes of spherical
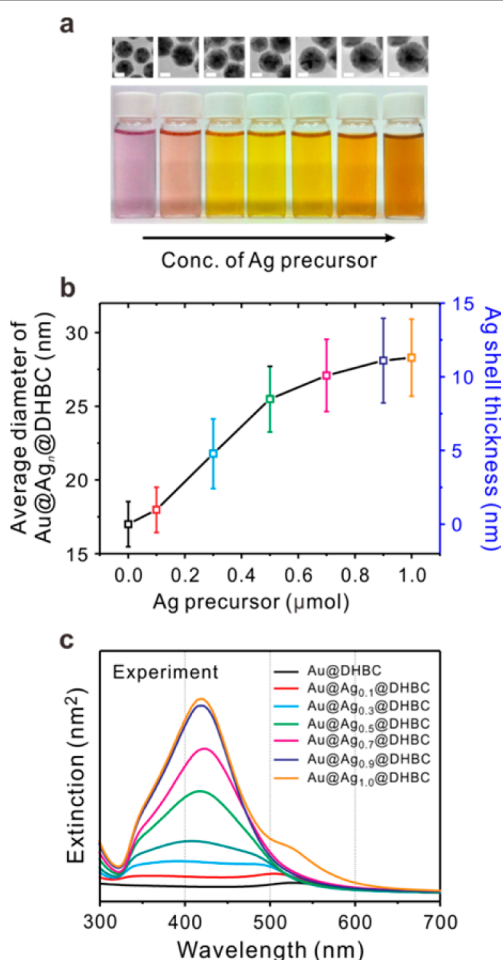

Figure 2. (a) (top) Series of TEM images and (bottom) their corresponding photographs of the Au@Ag@DHBC solution. The scale bar in the TEM images is 10 nm. (b) Average size of Au@Ag$_n$@DHBC NPs as a function of the concentration of Ag precursors (n = 0.0–1.0) and their corresponding Ag shell thickness. (c) UV–vis spectra collected for Au@Ag$_n$@DHBC NPs produced with different concentrations of Ag precursor (n = 0.0–1.0).

Ag nanostructures with different diameters.[50] The color difference also indicates that the Ag shell is homogeneously grown without particular transformation of structures. The thickness of the Ag shell can be efficiently tuned by controlling the amount of Ag precursor in solution. For example, as the concentration of Ag precursor is increased in the range from 0.1

to 1.0 μmol at a fixed concentration of Au@DHBC core, the average Ag shell thickness grows from 1.0 ± 1.54 to 11.3 ± 2.62 nm with a concomitant increase in the overall core–shell particle sizes from 17.0 ± 1.54 to 28.3 ± 2.62 nm (Figure 2b).

The absorption spectra display the plasmonic properties of core–shell NPs as a function of Ag shell thickness (Figure 2c). An increasing ratio of the Ag precursor to the Au seed can further lead to stronger plasmon absorption, and hence a new band at approximately 420 nm gradually appears, which eventually merges with the band at higher wavelengths of the Au@DHBC NPs. This result suggests that the uniform growth of the Ag shell on top of the Au@DHBC core can effectively modulate the plasmonic properties of Au@Ag@DHBC NPs. In accordance with results, we emphasize that isolated Au@Ag NPs with tunable shell thickness can be simply prepared by DHBC templates in solution. Because the SPR of metallic NPs is well-known to be highly sensitive to the surrounding environment, the formation of Ag shell on Au@DHBC NPs with tunable size can significantly influence the local electric field of Au@Ag@DHBC NPs. Thus, we simulated the electric field distribution using the three-dimensional finite-difference time-domain (FDTD) method to explore the electric field enhancement created by the Ag shell (Supporting Information Figure S4).[51] The results indicate that the plasmonic band changes of Au@Ag@DHBC NPs are in good agreement with those of the simulated spectra with Mie extinction calculations, even though the subtle differences between them are likely to arise from the polydispersity in the size and shape of the resulting NPs.

Interestingly, the SPR band at 420 nm gradually increases with the growth of the Ag shell up to a certain point, and then a new plasmon band at 520 nm begins to appear for Au@Ag$_{1.0}$@DHBC NPs. The former is attributed to the dipole oscillation of the isolated Au@Ag@DHBC NPs, whereas the latter is considered as a discrete plasmon absorption that requires more characterization to understand completely. Thus, we further investigated the structures and plasmonic properties of Au@Ag@DHBC NPs at higher concentrations of Ag precursor.

In the low concentration range (n < 0.9), the shell thickness of the isolated NPs consistently increased up to 11.1 nm (n = 0.9), which was similar to the theoretical chain length of the PEO block used in this study (~9.1 nm) (see Supporting Information for theoretical calculation).[52] In contrast, at the loading of 0.9 μmol of Ag precursor, the shell growth was slowed down, and the isolated NPs began to form disordered string-like nanostructures in solution (Supporting Information Figure S5). They continued to grow into large-sized clusters with increase in concentration of Ag precursor as shown in Figure 3. In the high concentration range (n > 0.9), the PEO block no longer assists the shell growth, but rather it provides a
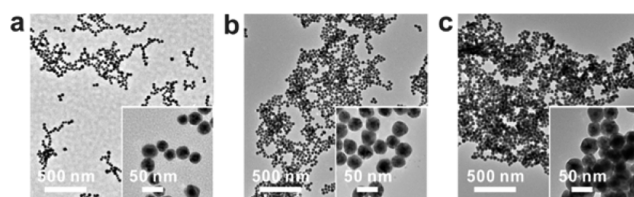

Figure 3. Coupled Au@Ag NPs by DHBC. (a–c) TEM images of Au@Ag@DHBC NPs synthesized by (a) 1.0, (b) 1.4, and (c) 1.8 μmol of Ag precursor, denoted as Au@Ag$_{1.0}$@DHBC, Au@Ag$_{1.4}$@DHBC, and Au@Ag$_{1.8}$@DHBC, respectively.

nanobridge between NPs, resulting in the interparticle coupling. Consequently, the coupled Au@Ag@DHBC NPs form cluster-like nanostructure instead of bulk agglomerates by the nanobridge between NPs. Thus, the PEO blocks in DHBC also play an essential role in this morphological transition of NPs as well as the Ag shell growth. This morphological change of NPs is significantly correlated with their plasmon feature, which will be discussed in the following section.

Recently, numerous studies on plasmon transition of NPs with their morphology have been reported. Single NPs generally have their intrinsic plasmonic absorption, e.g., a plasmon band at 520 nm of Au NP.[53] A dimer system with a nanogap generates a new longitudinal mode, whose dipolar response consistently red-shifts due to plasmon coupling when the particle separation is reduced further.[54] Because dimeric-like structure with nanogap is not physically contacted with neighboring NPs, no charge can be completely separated, leading to low-frequency mode attributed to the diverse plasmon mode such as antibonding dipolar, bonding dipolar, and quadrupolar mode.[55] These unphysical modes evolve into physical modes when the particle contact is made in the overlapping interparticles at a point. This overlapped particles show the low-frequency mode which is a true dipolar mode, giving rise to the charge transfer in the conductive junction of interparticles. Additionally, this mode blue-shifts when the overlap region is increased.[56−59] Similarly, in our Au@Ag@DHBC NPs, the new plasmon mode over 520 nm is expected to be induced by generation of conductive junction and corresponding diverse dipolar mode and charge separation (yellow region in Figure 4a). However, in contrast to the dimeric system with physical contact, this low-frequency mode

of Au@Ag@DHBC NPs consistently red-shifted toward near-infrared region as the concentration of Ag ions increases (C line in Figure 4b). One possible explanation is that Ag ions are consumed mostly to produce new junction between neighboring NPs as well as to increase the shell thickness of NPs at a high concentration of precursor. It is supported that no significant change is observed in the vertical length of the junction, when comparing with Au@Ag@DHBC NPs synthesized at high concentration of Ag precursor (Supporting Information Figure S6). On the other hand, the transverse plasmon mode remains steady (T line in Figure 4b) as the NPs maintain their spherical-like structure regardless of the increased concentration of Ag precursor. This morphological transition is accompanied by a colorimetric response of NPs, as a result of the change in plasmon coupling. The color of the solution turns to dark brown, which confirms the clustering of NPs. With a further increase in the concentration of Ag precursor ($n > 1.6$), the solution becomes transparent because the larger clusters eventually begin to precipitate out of the solution (inset in Figure 4b). Therefore, our current study can provide a method using DHBC templates for preparation of two types of Au@Ag@DHBC nanostructure including isolated NPs with different shell thickness and coupled NPs with tunable plasmon bands in solution.

We then studied the transition of core−shell Au@Ag@DHBC NPs via interparticle coupling to elucidate the detailed mechanism by collecting a series of TEM images and size distribution data using dynamic light scattering (DLS) at specific intervals. Au@Ag$_{1.6}$@DHBC NPs are employed as a model system because they exhibit two apparent and distinguishable absorption peaks. The collected solution at a specific time is diluted 40 times with water to quench the reaction, immediately followed by dropping the solution on a TEM grid, and dried in vacuum. As shown in Figure 5a, the Ag shell is uniformly grown on the surface of the Au@DHBC NPs without any byproducts after 5 min. Thereafter, new NPs with a diameter of several nanometers, which have rarely been observed in the growth of isolated Au@Ag@DHBC NPs, began to appear near the growing Au@Ag@DHBC NPs, while the thickness of the Ag shell consistently increased (10 min in Figure 5a). It is apparent that newly nucleated NPs consist of metallic Ag since their average diameter is much smaller than that of the Au seeds, and their electron density contrast is similar to that of the Ag shell of Au@Ag@DHBC NPs.

During the growth reaction from 15 to 30 min, it was observed that the population of the newly nucleated Ag NPs decreased, indicating that the Ag NPs independently moving in solution were absorbed and eventually merged into the Ag shell of Au@Ag@DHBC NPs. This integration is strongly attributed to Ostwald ripening, which is a dynamic process in solution to further grow the Ag shells. After the Ag shell had grown to a specific thickness, Ag NPs diffused into the adjacent Au@Ag@DHBC NPs at the same time, leading to coupling between isolated NPs after 45 min, as presented in Figure 5a. Each of the reaction steps, such as shell growth, new Ag NPs formation, and their integration into the Ag shell and interparticle coupling, obviously proceed at different time scales. However, we have discovered that these processes were not completely separated because small NPs less than 10.0 nm as well as large NPs of tens to hundreds of nanometers in size were observed according to the DLS measurements (10 and 30 min in Figure 5c). Furthermore, two strong size distributions at 60 min suggest the presence of isolated NPs as well as the formation of
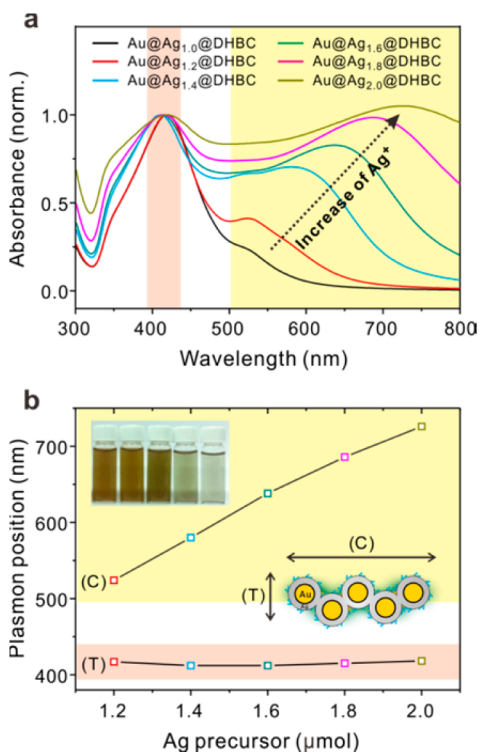

Figure 4. (a) UV−vis absorption spectra of Au@Ag@DHBC with Ag precursor concentrations in the range of 1.0 to 2.0 μmol and (b) the corresponding plasmon band plots of Au@Ag@DHBC NPs by transverse absorption (line T) and plasmon coupling (line C).
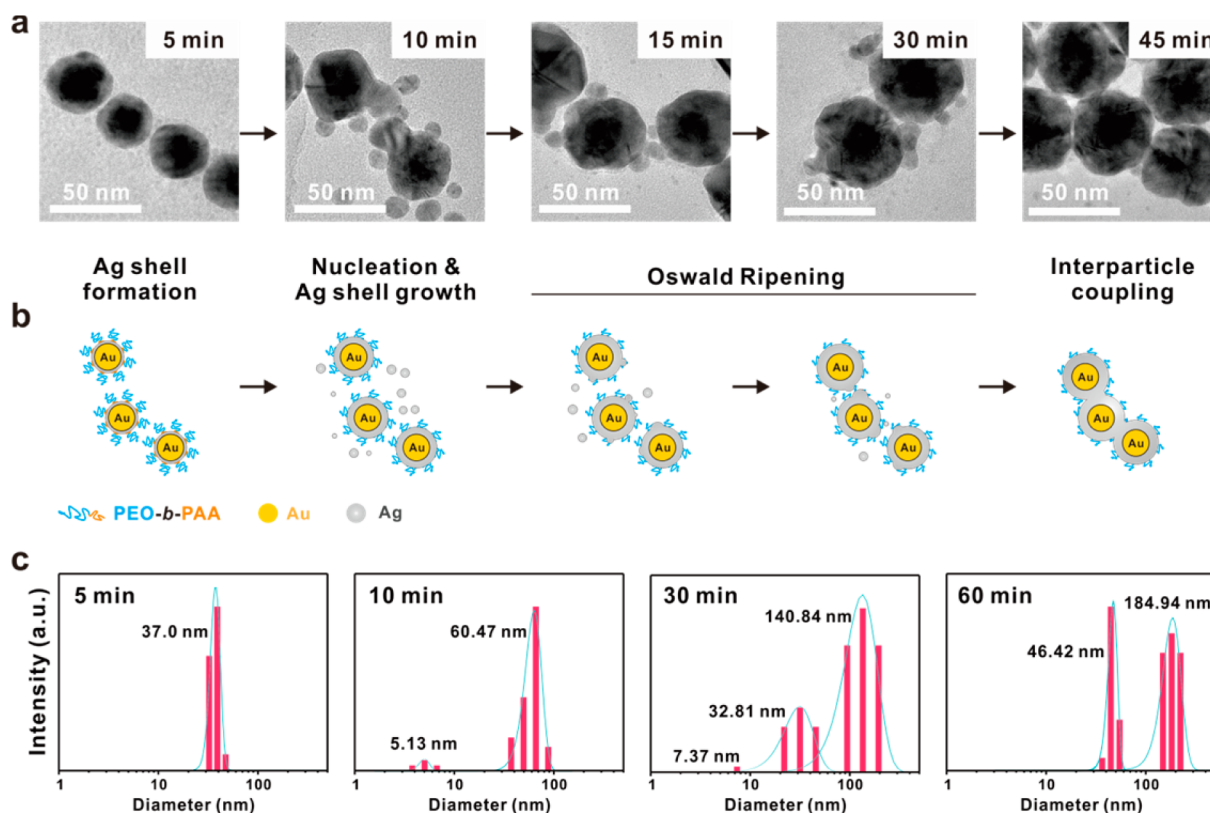
Figure 5. (a) Series of TEM images of Au@Ag$_{1.6}$@DHBC as a function of reaction time (5, 10, 15, 30, and 45 min). (b) Schematic drawings of the growth of the Ag layer and interparticle coupling. (c) Dynamic light scattering (DLS) analysis showing the hydrodynamic diameter changes during the growth of Au@Ag$_{1.6}$@DHBC NPs.

coupled NPs with various cluster sizes, indicating the heterogeneous interparticle coupling.

Considering all of these results, we propose a mechanism for the growth of core−shell type nanostructures and the further coupling of NPs based on the role of DHBC. At the initial stage, Au ions bind with the carboxylate groups of the PAA block through coordinative bonding, forming the micellar structure for spherical Au@DHBC NPs. Subsequently, the PEO block provides an active site to guide the formation of Ag shell on top of the Au core via ion−dipole interactions. Furthermore, free Ag NPs are nucleated from excess Ag ions in the solution and merged into the Ag shell of adjacent Au@Ag@ DHBC NPs by Ostwald ripening, leading to the interparticle coupling assisted by the presence of DHBC.

To evaluate the plasmonic effect of Au@Ag@DHBC NPs in PSCs, devices were fabricated with both isolated NPs (Au@ Ag$_{0.9}$@DHBC NPs) and coupled NPs (Au@Ag$_{1.6}$@DHBC NPs), and the control device was prepared without plasmonic NPs. To achieve high device performance, the devices were prepared by blending low band gap polymers, poly[4,8-bis(5-(2-ethylhexyl) thiophen-2-yl)benzo[1,2-b:4,5-b′] dithiophene-co-3-fluorothieno[3,4-b] thiophene-2-carboxylate] (PTB7-Th) as a donor and [6,6]-phenyl-C$_{71}$-butyric acid methyl ester (PC$_{71}$BM) as an acceptor, for the active layer. The information on the synthesis and photovoltaic properties of PTB7-Th has recently been reported.[60] The device structures are ITO/PEDOT:PSS/active layer/Al for the control device and ITO/PEDOT:PSS/Au@Ag@DHBC NPs/active layer/Al for the testing device (Figure 6a). More than 350 devices were prepared to optimize the device performance by controlling the concentration of NPs in the PTB7-Th:PC$_{71}$BM-based PSCs.

Any specific distinction in the morphology and thickness of the active layer is not observed after the incorporations of NPs into the system, which is confirmed using atomic force microscopy (AFM) and surface profiler (Supporting Information Figure S7).

Figure 6b,c shows current density−voltage (J−V) characteristics and incident photon-to-electron efficiency (IPCE), respectively, and the device parameters are summarized in Table 1. The best control device shows a short-circuit current (J$_{SC}$) of 14.53 mA/cm^2, an open-circuit voltage (V$_{OC}$) of 0.78 V, a fill factor of 0.68, and a power conversion efficiency (PCE) of 7.77%. The device with isolated NPs has a J$_{SC}$ of 15.78 mA/cm^2, V$_{OC}$ of 0.78 V, FF of 0.69, and PCE of 8.51%. The PCE value with approximately 9.5% enhancement for the device with isolated NPs can be primarily attributed to the increase in J$_{SC}$, which is caused by IPCE improvement in the 400−700 nm range, as shown in Figure 6c, whereas the FF is slightly increased. Furthermore, the device with coupled NPs shows a J$_{SC}$ of 16.28 mA/cm^2, V$_{OC}$ of 0.79 V, FF of 0.70, and PCE of 9.00%, exhibiting ∼16% enhancement in the PCE value. The enhanced PCE of the device with coupled NPs is attributed to the plasmon transition resulting from interparticle coupling, which is effective at broadening the absorption region as well as inducing stronger photon absorption and light scattering. Since little change in conductivity is expected by the addition of metal NPs,[23] the plasmonic effect of the NPs is considered as a main factor of the significant increases in PCE. We tested the device with Au@DHBC NPs only without Ag shell to confirm the plasmonic effect on the device. As similar to device performance with Au@Ag@DHBC NPs, the device incorporating with
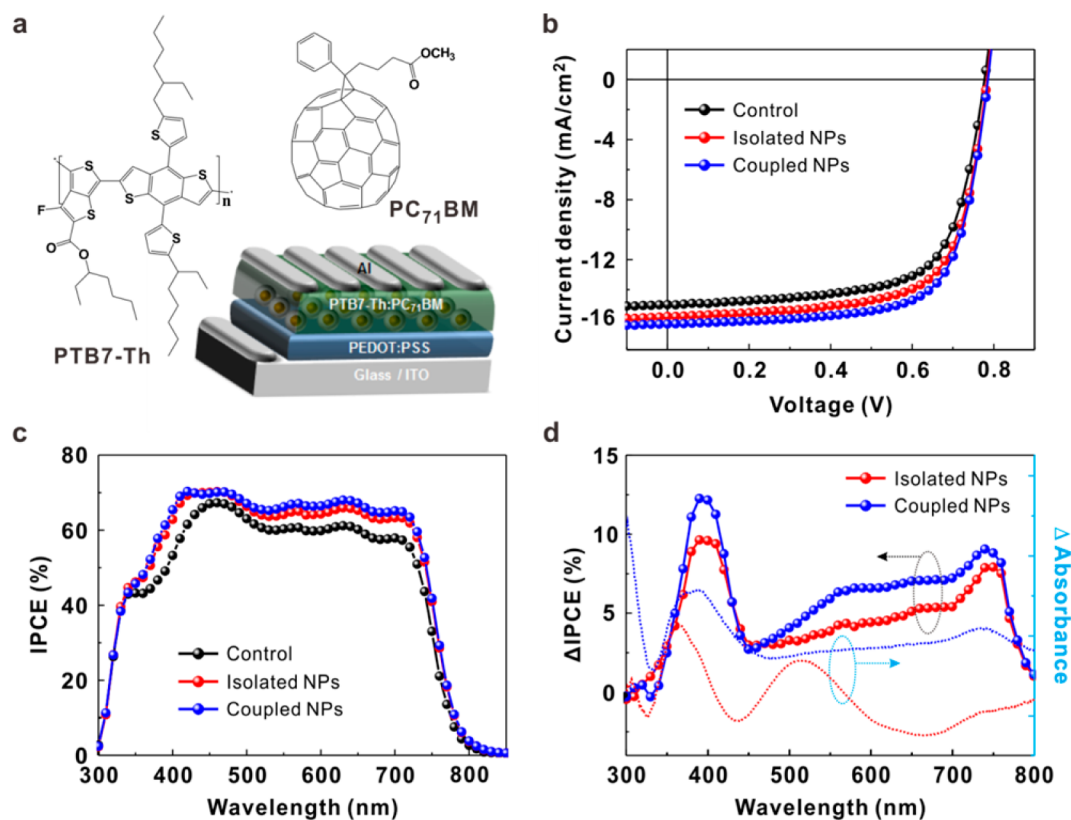
Figure 6. Device characteristics and spectral responses of plasmonic PSCs. (a) Schematic of polymer solar cell with chemical structures of PTB7-Th and PC$_{71}$BM, (b) current density–voltage (J–V) characteristics and (c) IPCE of a control device (black circles) and the best plasmonic PSCs with embedded Au@Ag@DHBC NPs (red and blue circles). (d) Comparison of enhanced IPCE and absorbance by Au@Ag@DHBC NPs.

Table 1. Device Characteristics of PTB7-Th:PC$_{71}$BM-Based PSCs with Au@Ag@DHBC NPs

device configuration	plasmonic NPs		J_{SC} (mA/cm^2)	V_{OC} (V)	FF	PCE (%)	J_{SC} [cal.] (mA/cm^2)
ITO/PEDOT:PSS/AL^a/Al	none (control)	best	14.53	0.78	0.68	7.77	14.41
		average	14.12 ± 0.41	0.78 ± 0.00	0.67 ± 0.01	7.37 ± 0.40	
ITO/PEDOT:PSS/isolated NPs/AL^a/Al	Au@Ag$_{0.9}$@DHBC	best	15.78	0.78	0.69	8.51	15.65
		average	15.38 ± 0.40	0.78 ± 0.00	0.69 ± 0.00	8.35 ± 0.19	
ITO/PEDOT:PSS/coupled NPs/AL^a/Al	Au@Ag$_{1.6}$@DHBC	best	16.28	0.79	0.70	9.00	16.08
		average	16.04 ± 0.24	0.78 ± 0.01	0.69 ± 0.01	8.74 ± 0.26	

^{a}AL: active layer consisting of PTB7-Th and PC$_{71}$BM.

Au@DHBC NPs shows the enhanced IPCE (3.1% enhancement) (Supporting Information Figure S8 and Table S1).

To clarify the plasmonic effect of isolated and coupled NPs on the photogeneration of charge carriers, we compared the enhanced IPCE (ΔIPCE) and absorbance (Δabsorbance) of the devices (Figure 6d). The IPCE enhancement of both devices with isolated and coupled NPs was found to show not only a strong absorption near 400 nm but also an extended absorption with broad visible and near-infrared region, which is consistent with the peaks in the difference of the absorbance spectrum.

For isolated NPs, the absorbance near 420 nm in solution is a unique feature, contributing to the enhancement of absorption near 400 nm on the device. Interestingly, the device with isolated NPs exhibits two discrete light absorptions near 530 nm and over 700 nm (Figure 6d), which may be attributed to the arrangement due to close spacing between the isolated NPs deposited on the film during device fabrication,[61] as characterized by AFM (Supporting Information Figure S9).

Particularly, the absorbance of the film near 530 nm leads to the improvement of light absorption on the device, which is considered to enhance the efficiency of the device with isolated NPs (Supporting Information Figure S10). The enhanced light absorption over 700 nm hardly contributes to the device efficiency because the light absorption by active layer in the near-infrared region is significantly lower than in the visible region (Figure 6c). On the other hand, the device with coupled NPs shows higher absorption in the full visible region (Figure 6d), compared with the device with isolated NPs. Moreover, it exhibits a similar tendency to change in the difference of ICPE, which is in agreement with absorption of coupled NPs in solution. Therefore, the incorporation of coupled NPs into the device is more advantageous for the enhancement of efficiency in PSCs, since an extended absorption into the visible region on the device with isolated NPs practically has a moderate effect on the device efficiency.

The light absorption in PSCs can be enhanced by light trapping by NPs with surface plasmon and scattering the

absorbed light by NPs.[2] To explore the contribution of absorption and scattering caused by NPs, we simulated the effect of NPs with different arrangements on the device. The results indicate that the incident light is simultaneously absorbed and scattered by NPs, but the effect of absorption of NPs on the device is much higher than that of light scattering (Supporting Information Figure S11). It implied the contribution of light absorption by NPs is relatively dominant for efficiency improvement in PSCs.[62]

It is remarkable that as-prepared NPs can be directly integrated into an active layer. We recently presented Ag NPs surrounded with a silica shell ($Ag@SiO_2$ NPs) to prevent exciton quenching[18] which often occurs when plasmonic NPs without any passivation layer come into direct contact with an active layer medium. However, we have found in our system that both isolated and coupled NPs can be successfully employed at the active interface with the aid of DHBC layers. To clearly elucidate the distinct feature of DHBC surrounding NPs against the quenching effect, we measured steady-state photoluminescence (PL) on film with the same thickness, including structures of Super Yellow (SY), PEDOT:PSS/SY, and PEDOT:PSS/isolated or coupled NPs/SY films coated on glass substrates. As a control test, SY films are fabricated with free Ag and Au NPs of similar diameter without DHBC (see Experimental Section and Supporting Information Figure S12). The PL intensities of PEDOT:PSS/isolated or coupled NPs/SY films are ∼7.4% and 11.0% higher than that of control PEDOT:PSS/SY film, respectively, whereas the PEDOT:PSS/ free Ag or Au NPs/SY film shows relatively lower PL intensity (decrease of 8.9 and 12.4%) than the film without NPs because of considerable exciton quenching at the interface of PEDOT:PSS/SY by the metal NPs (Supporting Information Figure S13).

Additionally, we measured the photoluminescence quantum efficiency (PLQE) of SY film of the same thickness for all samples to specifically support the PL results. The PLQE of SY films with isolated and coupled NPs exhibited higher values (12.36% and 13.64%, respectively) than those of the films with free Ag and Au NPs (10.78% and 10.07%, respectively), though the PLQE of the films with isolated and coupled NPs is lower than that of bare SY film due to strong exciton quenching effect induced by PEDOT:PSS layer (Table 2). This is in good

Table 2. PL Quantum Efficiency (PLQE) of Films with Different Configurations Measured inside an Integrating Sphere with an Excitation Wavelength of 470 nm

configuration	PLQE (%)
glass/SY[a]	19.79
glass/PEDOT:PSS/SY	11.83
glass/PEDOT:PSS/isolated NPs/SY	12.36
glass/PEDOT:PSS/coupled NPs/SY	13.64
glass/PEDOT:PSS/Ag NPs/SY	10.78
glass/PEDOT:PSS/Au NPs/SY	10.07

[a]Thickness of SY film: 30 nm.

agreement with steady-state PL results because the tendency of PLQE with and without NPs is well matched with that of PL spectra. It is obvious that PL quenching does not occur on devices incorporated with isolated and coupled NPs at the interface of PEDOT:PSS and active layer. This indicates that DHBC chains, which form a very thin layer on the surface of the NPs, provide a protective layer against exciton quenching,

resulting in plasmonic NPs that can be effectively integrated to a device. Therefore, we highlight that Au@Ag@DHBC NPs with a thin polymer layer can maximize the plasmonic effect via interparticle coupling within the active interface of PSCs, resulting in enhanced performance in PSC.

CONCLUSION

We have developed core−shell nanostructures using the double hydrophilic block copolymer (DHBC), PEO-*b*-PAA, as a soft template through coordinative and ion-dipole interactions between metal precursors and each segment of the DHBC. The DHBC used in this work is highly suitable to form core−shell nanostructures via the seed-mediated growth of NPs under mild ambient conditions. The PAA block of the DHBC forms micellar structures with the Au precursor and then induces a spherical Au core, whereas the PEO block provides the stability for nanoparticles in aqueous solution as well as guidance for uniform Ag shell growth. Moreover, this PEO block facilitates interparticle coupling, which leads to the transition of a new plasmon mode in the wide visible regions. The synthesized Au@Ag@DHBC NPs were successfully employed as plasmonic nanomaterials at the interface of an active layer, which considerably improved the efficiency of PSCs. We anticipate that DHBC-templated Au@Ag NPs would be widely applied as plasmonic materials in optoelectronic devices. In addition, this synthetic approach for the formation of NPs with DHBCs can lead to a facile and general method of producing core−shell nanostructures and tuning the intrinsic plasmonic effect of novel metal NPs for a variety of applications.

ASSOCIATED CONTENT

Ⓢ Supporting Information
Additional TEM (STEM) and AFM analysis, UV−vis spectra, PL spectra, simulation result, and calculation. The Supporting Information is available free of charge on the ACS Publications website at DOI: 10.1021/acs.chemmater.5b01591.

AUTHOR INFORMATION

Corresponding Authors
*(B.-S.K.) E-mail: bskim19@unist.ac.kr.
*(J.Y.K.) E-mail: jykim@unist.ac.kr.

Author Contributions
§(E.S. and S.-J.K.) These authors contributed equally.

Notes
The authors declare no competing financial interest.

REFERENCES

(1) Mayer, K. M.; Hafner, J. H. Localized Surface Plasmon Resonance Sensors. *Chem. Rev.* **2011**, *111*, 3828−3857.
(2) Atwater, H. A.; Polman, A. Plasmonics for Improved Photovoltaic Devices. *Nat. Mater.* **2010**, *9*, 205−213.

(3) Fan, J. A.; Wu, C.; Bao, K.; Bao, J.; Bardhan, R.; Halas, N. J.; Manoharan, V. N.; Nordlander, P.; Shvets, G.; Capasso, F. Self-Assembled Plasmonic Nanoparticle Clusters. *Science* 2010, 328, 1135−1138.

(4) Jana, N. R.; Gearheart, L.; Murphy, C. J. Seed-Mediated Growth Approach for Shape-Controlled Synthesis of Spheroidal and Rod-like Gold Nanoparticles Using a Surfactant Template. *Adv. Mater.* 2001, 13, 1389−1393.

(5) Zhao, Q.; Ji, M.; Qian, H.; Dai, B.; Weng, L.; Gui, J.; Zhang, J.; Ouyang, M.; Zhu, H. Controlling Structural Symmetry of a Hybrid Nanostructure and Its Effect on Efficient Photocatalytic Hydrogen Evolution. *Adv. Mater.* 2014, 26, 1387−1392.

(6) Wiley, B. J.; Im, S. H.; Li, Z.-Y.; McLellan, J.; Siekkinen, A.; Xia, Y. Maneuvering the Surface Plasmon Resonance of Silver Nanostructures through Shape-Controlled Synthesis. *J. Phys. Chem. B* 2006, 110, 15666−15675.

(7) DeSantis, C. J.; Weiner, R. G.; Radmilovic, A.; Bower, M. M.; Skrabalak, S. E. Seeding Bimetallic Nanostructures as a New Class of Plasmonic Colloids. *J. Phys. Chem. Lett.* 2013, 4, 3072−3082.

(8) Feng, Y.; He, J.; Wang, H.; Tay, Y. Y.; Sun, H.; Zhu, L.; Chen, H. An Unconventional Role of Ligand in Continuously Tuning of Metal−Metal Interfacial Strain. *J. Am. Chem. Soc.* 2012, 134, 2004−2007.

(9) Kang, Y.; Erickson, K. J.; Taton, T. A. Plasmonic Nanoparticle Chains via a Morphological, Sphere-to-String Transition. *J. Am. Chem. Soc.* 2005, 127, 13800−13801.

(10) Mulvihill, M. J.; Ling, X. Y.; Henzie, J.; Yang, P. Anisotropic Etching of Silver Nanoparticles for Plasmonic Structures Capable of Single-Particle SERS. *J. Am. Chem. Soc.* 2009, 132, 268−274.

(11) Cho, E. C.; Choi, S.-W.; Camargo, P. H.; Xia, Y. Thiol-Induced Assembly of Au Nanoparticles into Chainlike Structures and Their Fixing by Encapsulation in Silica Shells or Gelatin Microspheres. *Langmuir* 2010, 26, 10005−10012.

(12) Yang, M.; Chen, G.; Zhao, Y.; Silber, G.; Wang, Y.; Xing, S.; Han, Y.; Chen, H. Mechanistic Investigation into the Spontaneous Linear Assembly of Gold Nanospheres. *Phys. Chem. Chem. Phys.* 2010, 12, 11850−11860.

(13) Peng, S.; McMahon, J. M.; Schatz, G. C.; Gray, S. K.; Sun, Y. Reversing the Size-Dependence of Surface Plasmon Resonances. *Proc. Natl. Acad. Sci. U. S. A.* 2010, 107, 14530−14534.

(14) Jiang, R.; Chen, H.; Shao, L.; Li, Q.; Wang, J. Unraveling the Evolution and Nature of the Plasmons in (Au Core)−(Ag Shell) Nanorods. *Adv. Mater.* 2012, 24, OP200−OP207.

(15) Kelly, K. L.; Coronado, E.; Zhao, L. L.; Schatz, G. C. The Optical Properties of Metal Nanoparticles: The Influence of Size, Shape, and Dielectric Environment. *J. Phys. Chem. B* 2003, 107, 668−677.

(16) Jang, L. W.; Jeon, D. W.; Kim, M.; Jeon, J. W.; Polyakov, A. Y.; Ju, J. W.; Lee, S. J.; Baek, J. H.; Yang, J. K.; Lee, I. H. Investigation of Optical and Structural Stability of Localized Surface Plasmon Mediated Light-Emitting Diodes by Ag and Ag/SiO₂ Nanoparticles. *Adv. Funct. Mater.* 2012, 22, 2728−2734.

(17) Zhang, L.; Song, Y.; Fujita, T.; Zhang, Y.; Chen, M.; Wang, T. H. Large Enhancement of Quantum Dot Fluorescence by Highly Scalable Nanoporous Gold. *Adv. Mater.* 2013, 26, 1289−1294.

(18) Choi, H.; Lee, J.-P.; Ko, S.-J.; Jung, J.-W.; Park, H.; Yoo, S.; Park, O.; Jeong, J.-R.; Park, S.; Kim, J. Y. Multipositional Silica-Coated Silver Nanoparticles for High-Performance Polymer Solar Cells. *Nano Lett.* 2013, 13, 2204−2208.

(19) Sotiriou, G. A.; Sannomiya, T.; Teleki, A.; Krumeich, F.; Vörös, J.; Pratsinis, S. E. Non-Toxic Dry-Coated Nanosilver for Plasmonic Biosensors. *Adv. Funct. Mater.* 2010, 20, 4250−4257.

(20) Nam, J.; Won, N.; Jin, H.; Chung, H.; Kim, S. pH-Induced Aggregation of Gold Nanoparticles for Photothermal Cancer Therapy. *J. Am. Chem. Soc.* 2009, 131, 13639−13645.

(21) Wang, Y.; Liu, Y.; Luehmann, H.; Xia, X.; Wan, D.; Cutler, C.; Xia, Y. Radioluminescent Gold Nanocages with Controlled Radioactivity for Real-Time in vivo Imaging. *Nano Lett.* 2013, 13, 581−585.

(22) Samal, A. K.; Polavarapu, L.; Rodal-Cedeira, S.; Liz-Marzán, L. M.; Pérez-Juste, J.; Pastoriza-Santos, I. Size Tunable Au@Ag Core−Shell Nanoparticles: Synthesis and Surface-Enhanced Raman Scattering Properties. *Langmuir* 2013, 29, 15076−15082.

(23) Yang, J.; You, J.; Chen, C.-C.; Hsu, W.-C.; Tan, H.-r.; Zhang, X. W.; Hong, Z.; Yang, Y. Plasmonic Polymer Tandem Solar Cell. *ACS Nano* 2011, 5, 6210−6217.

(24) Lu, L.; Luo, Z.; Xu, T.; Yu, L. Cooperative Plasmonic Effect of Ag and Au Nanoparticles on Enhancing Performance of Polymer Solar Cells. *Nano Lett.* 2012, 13, 59−64.

(25) Wang, D. H.; Park, K. H.; Seo, J. H.; Seifter, J.; Jeon, J. H.; Kim, J. K.; Park, J. H.; Park, O. O.; Heeger, A. J. Enhanced Power Conversion Efficiency in PCDTBT/PC₇₀BM Bulk Heterojunction Photovoltaic Devices with Embedded Silver Nanoparticle Clusters. *Adv. Energy Mater.* 2011, 1, 766−770.

(26) Wang, D. H.; Kim, D. Y.; Choi, K. W.; Seo, J. H.; Im, S. H.; Park, J. H.; Park, O. O.; Heeger, A. J. Enhancement of Donor-Acceptor Polymer Bulk Heterojunction Solar Cell Power Conversion Efficiencies by Addition of Au Nanoparticles. *Angew. Chem., Int. Ed.* 2011, 50, 5519−5523.

(27) Baek, S.-W.; Park, G.; Noh, J.; Cho, C.; Lee, C.-H.; Seo, M.-K.; Song, H.; Lee, J.-Y. Au@Ag Core-Shell Nanocubes for Efficient Plasmonic Light Scattering Effect in Low Bandgap Organic Solar Cells. *ACS Nano* 2014, 8, 3302−3312.

(28) Jankovic, V.; Yang, Y.; You, J.; Dou, L.; Liu, Y.; Cheung, P.; Chang, J. P. Active Layer-Incorporated, Spectrally Tuned Au/SiO₂ Core/Shell Nanorod-Based Light Trapping for Organic Photovoltaics. *ACS Nano* 2013, 7, 3815−3822.

(29) Wu, J.-L.; Chen, F.-C.; Hsiao, Y.-S.; Chien, F.-C.; Chen, P.; Kuo, C.-H.; Huang, M. H.; Hsu, C.-S. Surface Plasmonic Effects of Metallic Nanoparticles on the Performance of Polymer Bulk Heterojunction Solar Cells. *ACS Nano* 2011, 5, 959−967.

(30) Li, X.; Choy, W. C. H.; Lu, H.; Sha, W. E.; Ho, A. H. P. Efficiency Enhancement of Organic Solar Cells by Using Shape-Dependent Broadband Plasmonic Absorption in Metallic Nanoparticles. *Adv. Funct. Mater.* 2013, 23, 2728−2735.

(31) Choi, H.; Ko, S. J.; Choi, Y.; Joo, P.; Kim, T.; Lee, B. R.; Jung, J. W.; Choi, H. J.; Cha, M.; Jeong, J. R.; Hwang, I. W.; Song, M. H.; Kim, B. S.; Kim, J. Y. Versatile Surface Plasmon Resonance of Carbon-Dot-Supported Silver Nanoparticles in Polymer Optoelectronic Devices. *Nat. Photonics* 2013, 7, 732−738.

(32) Xu, H.; Xu, Y.; Pang, X.; He, Y.; Jung, J.; Xia, H.; Lin, Z. A General Route to Nanocrystal Kebabs Periodically Assembled on Stretched Flexible Polymer Shish. *Sci. Adv.* 2015, 1, e1500025.

(33) Pang, X.; Zhao, L.; Feng, C.; Lin, Z. Novel Amphiphilic Multiarm, Starlike Coil−Rod Diblock Copolymers via a Combination of Click Chemistry with Living Polymerization. *Macromolecules* 2011, 44, 7176−7183.

(34) Xu, H.; Pang, X.; He, Y.; He, M.; Jung, J.; Xia, H.; Lin, Z. An Unconventional Route to Monodisperse and Intimately Contacted Semiconducting Organic−Inorganic Nanocomposites. *Angew. Chem.* 2015, 127, 4719−4723.

(35) Mistark, P. A.; Park, S.; Yalcin, S. E.; Lee, D. H.; Yavuzcetin, O.; Tuominen, M. T.; Russell, T. P.; Achermann, M. Block-Copolymer-Based Plasmonic Nanostructures. *ACS Nano* 2009, 3, 3987−3992.

(36) Shin, D. O.; Mun, J. H.; Hwang, G.-T.; Yoon, J. M.; Kim, J. Y.; Yun, J. M.; Yang, Y.-B.; Oh, Y.; Lee, J. Y.; Shin, J.; Lee, K. J.; Park, S.; Kim, J. U.; Kim, S. O. Multicomponent Nanopatterns by Directed Block Copolymer Self-Assembly. *ACS Nano* 2013, 7, 8899−8907.

(37) Leong, W. L.; Lee, P. S.; Lohani, A.; Lam, Y. M.; Chen, T.; Zhang, S.; Dodabalapur, A.; Mhaisalkar, S. G. Non-Volatile Organic Memory Applications Enabled by in situ Synthesis of Gold Nanoparticles in a Self-Assembled Block Copolymer. *Adv. Mater.* 2008, 20, 2325−2331.

(38) Wang, L.; Yamauchi, Y. Autoprogrammed Synthesis of Triple-Layered Au@Pd@Pt Core-Shell Nanoparticles Consisting of a Au@Pd Bimetallic Core and Nanoporous Pt Shell. *J. Am. Chem. Soc.* 2010, 132, 13636−13638.

(39) Pang, X. C.; Zhao, L.; Han, W.; Xin, X. K.; Lin, Z. Q. A General and Robust Strategy for the Synthesis of Nearly Monodisperse Colloidal Nanocrystals. *Nat. Nanotechnol.* 2013, 8, 426−431.

(40) Bastakoti, B. P.; Guragain, S.; Yusa, S.; Nakashima, K. Novel Synthesis Route for Ag@SiO$_2$ Core-Shell Nanoparticles via Micelle Template of Double Hydrophilic Block Copolymer. *RSC Adv.* **2012**, *2*, 5938−5940.

(41) Bastakoti, B. P.; Sukegawa, H.; Wu, K. C. W.; Yamauchi, Y. Synthesis of Porous Iron Oxide Microspheres by a Double Hydrophilic Block Copolymer. *RSC Adv.* **2014**, *4*, 9986−9989.

(42) Nakashima, K.; Bahadur, P. Aggregation of Water-Soluble Block Copolymers in Aqueous Solutions: Recent Trends. *Adv. Colloid Interface Sci.* **2006**, *123*, 75−96.

(43) Colfen, H. Double-Hydrophilic Block Copolymers: Synthesis and Application as Novel Surfactants and Crystal Growth Modifiers. *Macromol. Rapid Commun.* **2001**, *22*, 219−252.

(44) Seo, E.; Kim, J.; Hong, Y.; Kim, Y. S.; Lee, D.; Kim, B.-S. Double Hydrophilic Block Copolymer Templated Au Nanoparticles with Enhanced Catalytic Activity toward Nitroarene Reduction. *J. Phys. Chem. C* **2013**, *117*, 11686−11693.

(45) Palik, E. D. *Handbook of Optical Constants of Solids*; Academic Press: 1998; Vol. *3*.

(46) Luo, C.; Zhang, Y.; Zeng, X.; Zeng, Y.; Wang, Y. The Role of Poly(ethylene glycol) in the Formation of Silver Nanoparticles. *J. Colloid Interface Sci.* **2005**, *288*, 444−448.

(47) Voronov, A.; Kohut, A.; Vasylyev, S.; Peukert, W. Mechanism of Silver Ion Reduction in Concentrated Solutions of Amphiphilic Invertible Polyesters in Nonpolar Solvent at Room Temperature. *Langmuir* **2008**, *24*, 12587−12594.

(48) Jeong, S.; Woo, K.; Kim, D.; Lim, S.; Kim, J. S.; Shin, H.; Xia, Y.; Moon, J. Controlling the Thickness of the Surface Oxide Layer on Cu Nanoparticles for the Fabrication of Conductive Structures by Ink-Jet Printing. *Adv. Funct. Mater.* **2008**, *18*, 679−686.

(49) Washio, I.; Xiong, Y.; Yin, Y.; Xia, Y. Reduction by the End Groups of Poly(vinyl pyrrolidone): A New and Versatile Route to the Kinetically Controlled Synthesis of Ag Triangular Nanoplates. *Adv. Mater.* **2006**, *18*, 1745−1749.

(50) Zhang, Q.; Xie, J.; Yang, J.; Lee, J. Y. Monodisperse Icosahedral Ag, Au, and Pd Nanoparticles: Size Control Strategy and Superlattice Formation. *ACS Nano* **2009**, *3*, 139−148.

(51) Wen, F.; Ye, J.; Liu, N.; Van Dorpe, P.; Nordlander, P.; Halas, N. J. Plasmon Transmutation: Inducing New Modes in Nanoclusters by Adding Dielectric Nanoparticles. *Nano Lett.* **2012**, *12*, 5020−5026.

(52) He, J.; Liu, Y.; Babu, T.; Wei, Z.; Nie, Z. Self-Assembly of Inorganic Nanoparticle Vesicles and Tubules Driven by Tethered Linear Block Copolymers. *J. Am. Chem. Soc.* **2012**, *134*, 11342−11345.

(53) Jana, N. R.; Gearheart, L.; Murphy, C. J. Seeding Growth for Size Control of 5−40 nm Diameter Gold Nanoparticles. *Langmuir* **2001**, *17*, 6782−6786.

(54) Talley, C. E.; Jackson, J. B.; Oubre, C.; Grady, N. K.; Hollars, C. W.; Lane, S. M.; Huser, T. R.; Nordlander, P.; Halas, N. J. Surface-Enhanced Raman Scattering from Individual Au Nanoparticles and Nanoparticle Dimer Substrates. *Nano Lett.* **2005**, *5*, 1569−1574.

(55) Lee, H.; Lee, J.-H.; Jin, S. M.; Suh, Y. D.; Nam, J.-M. Single-Molecule and Single-Particle-Based Correlation Studies between Localized Surface Plasmons of Dimeric Nanostructures with ∼1 nm Gap and Surface-Enhanced Raman Scattering. *Nano Lett.* **2013**, *13*, 6113−6121.

(56) Atay, T.; Song, J.-H.; Nurmikko, A. V. Strongly Interacting Plasmon Nanoparticle Pairs: From Dipole-Dipole Interaction to Conductively Coupled Regime. *Nano Lett.* **2004**, *4*, 1627−1631.

(57) Lassiter, J. B.; Aizpurua, J.; Hernandez, L. I.; Brandl, D. W.; Romero, I.; Lal, S.; Hafner, J. H.; Nordlander, P.; Halas, N. J. Close Encounters between Two Nanoshells. *Nano Lett.* **2008**, *8*, 1212−1218.

(58) Lee, J.-H.; You, M.-H.; Kim, G.-H.; Nam, J.-M. Plasmonic Nanosnowmen with a Conductive Junction as Highly Tunable Nanoantenna Structures and Sensitive, Quantitative and Multiplexable Surface-Enhanced Raman Scattering Probes. *Nano Lett.* **2014**, *14*, 6217−6225.

(59) Romero, I.; Aizpurua, J.; Bryant, G. W.; García De Abajo, F. J. Plasmons in Nearly Touching Metallic Nanoparticles: Singular Response in the Limit of Touching Dimers. *Opt. Express* **2006**, *14*, 9988−9999.

(60) Liao, S.-H.; Jhuo, H.-J.; Cheng, Y.-S.; Chen, S.-A. Fullerene Derivative-Doped Zinc Oxide Nanofilm as the Cathode of Inverted Polymer Solar Cells with Low-Bandgap Polymer (PTB7-Th) for High Performance. *Adv. Mater.* **2013**, *25*, 4766−4771.

(61) Nakayama, K.; Tanabe, K.; Atwater, H. A. Plasmonic Nanoparticle Enhanced Light Absorption in GaAs Solar Cells. *Appl. Phys. Lett.* **2008**, *93*, 121904.

(62) Ko, S.-J.; Choi, H.; Lee, W.; Kim, T.; Lee, B. R.; Jung, J.-W.; Jeong, J.-R.; Song, M. H.; Lee, J. C.; Woo, H. Y.; Kim, J. Y. Highly Efficient Plasmonic Organic Optoelectronic Devices based on a Conducting Polymer Electrode Incorporated with Silver Nanoparticles. *Energy Environ. Sci.* **2013**, *6*, 1949−1955.